How interaction radius shapes vortex states in mobile phase oscillators

Jingtian Shang,[1,2] Yingshan Guo,[1,3] Zhigang Zheng,[1,4,*] and Changgui Gu[5,†]
[1]*Institute of Systems Science, Huaqiao University, Xiamen 361021, China*
[2]*School of Mathematical Sciences, Huaqiao University, Quanzhou 362021, China*
[3]*College of Mechanical Engineering and Automation, Huaqiao University, Xiamen 361021, China*
[4]*College of Information Science and Engineering, Huaqiao University, Xiamen 361021, China*
[5]*Business School, University of Shanghai for Science and Technology, Shanghai 200093, China*

(Received 6 June 2026; accepted 16 October 2026; published 4 November 2026)

Vortex patterns are a prominent form of collective organization in chiral active matter, yet how local interactions affect their persistence and eventual breakdown has not been fully clarified. We investigate vortex states in the Vicsek-Kuramoto model with different interaction ranges. For locally interacting mobile phase oscillators, vortex states persist over finite intervals of the coupling strength and are eventually replaced by the polar ordered state as the coupling strength increases. Adiabatic scans of the coupling strength reveal the coexistence of vortex and polar ordered states and lead to pronounced hysteresis, indicating that vortex states act as stable dynamical attractors rather than transient structures. To understand these behaviors, we combine continuum theory with linear stability analysis and show that the incoherent state first becomes unstable through the zero-wave-number mode, with a critical coupling strength identical to that of the classical Kuramoto model. By deriving the critical coupling strengths for the homogeneous mode and finite-wave-number modes, we demonstrate how the interaction range controls the separation of instability thresholds. These results characterize the dependence of collective states on the interaction radius and quantify its influence on the linear instability conditions of the incoherent state in the Vicsek-Kuramoto model.

DOI: 10.1103/mzgk-nx4w

I. INTRODUCTION

Synchronization is a fundamental collective phenomenon observed across a wide range of physical, chemical, biological, and engineered systems, including systems such as Josephson junction arrays [1], chemical turbulence [2] and mechanical oscillators [3,4], as well as engineering applications such as power grids [5], bridge vibrations [6], and coupled laser arrays [7]. In systems of interacting mobile agents, synchronization can also manifest as coordinated behavior at the level of interacting groups, particularly in biological systems such as starling flocks [8,9], fish schools [10,11], microswimmers like sperm and vinegar eels [12,13], and robot systems [14]. This collective perspective on synchronization provides an important macroscopic context for the study of collective motion and complex collective behavior.

In the context of mobile agent systems, a central question is whether locally interacting moving units can develop a common direction of motion over large spatial scales. Early theoretical work by Toner and Tu showed that such large-scale directional alignment, known as long-range polar order, can persist even in two-dimensional systems [15–17]. This result established the homogeneous polar ordered state as a natural reference state for collective motion. However, extensive observational and computational studies have shown that many biological and synthetic systems also organize into spatially structured configurations characterized by rotation and circulation. Vortex patterns have been reported in a variety of systems, including milling behavior in fish schools [18–20], enhanced angular polarization in insect swarms [21,22], and torus states in bird flocks [23]. A particularly striking example is the ant death vortex, which can arise in army ant colonies under specific conditions [24,25]. Comparable circulating and vortex patterns have also been observed in bacterial suspensions and other spatially extended interacting systems [26–29].

To account for these diverse forms of collective behavior, a variety of theoretical models have been developed to capture different aspects of collective dynamics in interacting many-agent systems. The Kuramoto model [30–32] provides an analytically tractable framework for studying phase synchronization in populations of coupled oscillators, while the Vicsek model [33–35] captures alignment-driven collective motion in systems of self-propelled particles. Building on these two seminal approaches, hybrid frameworks such as the Vicsek-Kuramoto model [36–39] and the swarmalator model [40–44] combine spatial motion with internal phase dynamics to describe collective behaviors of interacting agents. These

*Contact author: zgzheng@hqu.edu.cn
†Contact author: gu_changgui@163.com

Published by the American Physical Society under the terms of the Creative Commons Attribution 4.0 International license. Further distribution of this work must maintain attribution to the author(s) and the published article's title, journal citation, and DOI.

hybrid models provide a theoretical setting to study how internal synchronization and spatial motion coevolve and how their coupling shapes emergent collective patterns.

In mobile agent systems, interactions are typically local in space, so collective order is shaped by finite neighborhoods rather than by global mean-field coupling [45,46]. Because motion and activity continuously modify who interacts with whom, locality couples transport to ordering and makes spatiotemporal organization a generic outcome [47,48]. Consequently, spatially propelling agents with locally interacting phase dynamics provide a natural theoretical setting for studying patterned collective states beyond polar ordered states [49–51]. Despite this broad recognition of locality, many studies adopt a fixed sensing radius and do not treat the interaction range itself as a primary control parameter to be extensively scanned. The exploration of swarmalators has only recently begun to investigate tunable coupling ranges explicitly, showing that reducing the interaction range can generate qualitatively new collective states and phase boundaries [52,53].

The relevance of finite-range constraints is also evident in engineered mobile systems such as unmanned aerial vehicle (UAV) swarms. In such systems, the sensing range determines which neighboring agents or targets can be observed, whereas the communication range determines which agents can directly exchange information. Changes in sensing or communication range can therefore modify the available neighborhood of each UAV and influence cooperative tracking, formation control, and collective coordination [54–57]. These examples further indicate that the interaction range is not merely a technical modeling parameter, but a physically and practically meaningful quantity in mobile agent systems.

Compared with previous work on activity-induced synchronization and chiral self-sorting, our contributions are twofold. Numerically, we systematically map the coupling intervals supporting persistent vortex states, show that these intervals narrow as the interaction radius increases within the parameter range examined, and identify coexistence and hysteresis between vortex and polar ordered states. The coexistence and hysteresis provide numerical evidence for multiple dynamical attractors at the same parameter values. Theoretically, we derive a dispersion relation for perturbations of the homogeneous incoherent state within a continuum linear approximation that incorporates particle transport and finite-range coupling. For a Lorentzian frequency distribution, the homogeneous instability threshold $K_c(0) = 2\Delta$ is independent of the interaction radius d_0, whereas the finite-wave-number thresholds $K_c(q, d_0)$ depend on d_0. Physically, normalized neighborhood averaging preserves the coupling response of homogeneous perturbations while filtering spatially nonuniform perturbations according to their spatial scale. This modifies their growth conditions and provides qualitative insight into the spatial structures observed numerically.

The paper is organized as follows. In Sec. II, we introduce the model and define the relevant order parameters. In Sec. III, we study the formation and persistence of vortex states, focusing on pattern evolution and the transition from vortex states to polar ordered states as the coupling strength increases. In Sec. IV, we characterize the persistence of vortex states and their coexistence with polar ordered states through adiabatic scans of the coupling strength, revealing pronounced hysteresis behavior. In Sec. V, we analyze the linear instability of the incoherent state, derive the critical coupling strengths associated with the zero- and lowest nonzero-wave-number modes, and show how the separation between their instability thresholds depends on the interaction range. In Sec. VI, we examine the dependence of collective states on particle number and system size by varying the particle number at fixed system size and enlarging the domain at fixed density. Finally, the conclusions are drawn in Sec. VII.

II. VICSEK-KURAMOTO MODEL WITH FINITE-RANGE INTERACTIONS

We consider a noiseless system of mobile phase oscillators whose microscopic dynamics combine Vicsek-type self-propulsion [33] with Kuramoto-type sinusoidal phase coupling [30]. Each oscillator moves at a constant speed along a direction determined by its phase, so that the phase represents both an internal state and the heading direction [37,38]. Oscillators interact locally with neighbors within the interaction radius d_0. The dynamical equations are given by

$$\dot{\mathbf{x}}_i = v\mathbf{n} = v(\cos\theta_i, \sin\theta_i), \tag{1}$$

$$\dot{\theta}_i = \omega_i + \frac{K}{N_i}\sum_{j\in d_0}\sin(\theta_j - \theta_i). \tag{2}$$

Here, $\mathbf{x}_i = (x_i, y_i)$ denotes the position of the ith oscillator in two-dimensional space and $\dot{\mathbf{x}}_i$ is its instantaneous velocity. The constant v is the self-propulsion speed. The unit vector $\mathbf{n}_i$ specifies the direction of motion and is determined by the phase $\theta_i \in [0, 2\pi)$. We consider agents moving in a two-dimensional square domain of size $L \times L$ with periodic boundary conditions. Distances d_{ij} are computed from the shortest periodic displacement between two agents:

$$d_{ij} = \sqrt{\Delta x_{ij}^2 + \Delta y_{ij}^2}, \tag{3}$$

where $\Delta x_{ij} = \min(|x_i - x_j|,\ L - |x_i - x_j|)$, $\Delta y_{ij} = \min(|y_i - y_j|,\ L - |y_i - y_j|)$.

Furthermore, the adjacency relationship between oscillators is determined by their mutual distances. Accordingly, the elements of the adjacency matrix A_{ij} are defined based on the spatial distance d_{ij} between oscillators i and j as

$$A_{ij} = \begin{cases} 1, & \text{if } d_{ij} \leqslant d_0, \\ 0, & \text{if } d_{ij} > d_0. \end{cases} \tag{4}$$

The second term in Eq. (2) describes a Kuramoto-type local coupling with its strength K. This implies that interactions exist only among oscillators located within the interaction range d_0; namely, oscillator i interacts with oscillator j if $d_{ij} \leqslant d_0$. Here, N_i denotes the number of such neighboring oscillators.

The natural frequencies $\{\omega_i\}$ are drawn from a Lorentzian distribution centered at zero,

$$g(\omega) = \frac{\Delta}{\pi(\omega^2 + \Delta^2)}. \tag{5}$$

Here, Δ is the half width at half maximum and characterizes the degree of frequency heterogeneity. The Lorentzian distribution is chosen primarily for analytical tractability: Its simple pole structure allows the frequency integrals arising in the linear stability analysis to be evaluated exactly using residue calculus, thereby yielding closed-form expressions for the instability thresholds of both homogeneous and finite-wave-number modes.

To quantify global phase coherence, we use the standard Kuramoto order parameter [31], defined as

$$R_G = \frac{1}{N}\sum_{j=1}^{N} e^{i\theta_j}. \tag{6}$$

$R_G \approx 1$ represents the fully synchronized state of oscillator phases, while $R_G \approx 0$ corresponds to a disordered phase state. To characterize local phase coherence, we define a complex local order parameter using a normalized average over the interaction neighborhood [39],

$$Z(\mathbf{x}, t) = R(\mathbf{x}, t)e^{i\psi(\mathbf{x},t)} = \frac{1}{N_i}\sum_{j\in d_0} e^{i\theta_j}, \tag{7}$$

which characterizes the degree of local synchronization through its modulus and mean phase within the interaction range d_0.

III. DYNAMICS OF VORTEX STATES

We investigate the dynamical behavior of the proposed model through numerical simulations and find that it exhibits a variety of collective states across different parameter regimes. After discarding the initial transient, we compute and display the time series of the global order parameter $R_G(t)$ over the final 100 dimensionless time units to characterize the temporal evolution of global synchronization. More importantly, the model describes a motion-induced, time-varying interaction network A_{ij}, whose topology is not fixed in advance but instead emerges self-consistently from the agents' spatial motion. As a consequence, monitoring the network structure itself is crucial for a proper understanding of system dynamics. The adjacency matrix A_{ij} corresponds to the same instantaneous snapshot. Nodes are reordered according to their natural frequencies in ascending order to visualize the instantaneous connectivity structure.

A. Formation of vortex states

Motivated by these observations, we proceed to investigate how the coupling strength K affects the asymptotic dynamical states of the system for a fixed interaction radius d_0. By comparing representative snapshots, order parameters, and interaction networks, we identify a progression of regimes from disordered motion to vortex states and eventually to a polar ordered state as the coupling strength increases.

At weak coupling $K = 0.1$, the system exhibits a vortex-like state. As shown in Fig. 1(a), mobile phase oscillators are broadly distributed across the domain, without forming well-defined spatial clusters. The snapshot shows a spatially heterogeneous phase field with multicolored phase values and locally varying arrow directions. The phase distribution is disordered across the domain, and arrow directions vary strongly from place to place, with only a weakly organized curved arrangement around the central area. Consistent with the spatial snapshot, the global order parameter $R_G(t)$, shown in Fig. 1(b), remains close to zero over the entire observation window, exhibiting only small amplitude fluctuations and indicating the absence of macroscopic coherence. From the adjacency matrix in Fig. 1(c), oscillators exhibit large variations in the number of neighbors at weak coupling. Some oscillators interact with many neighbors, whereas others have relatively few. Overall, the system remains in a disordered regime with incoherent phases, low global order, and a scattered connectivity structure.

At a moderate coupling strength $K = 1$, the system exhibits a vortex state. As shown in Fig. 1(d), the spatial snapshot reveals the emergence of two well-defined vortex structures, forming a double-vortex configuration. The mobile phase oscillators are spatially organized into two rotating groups, each circulating around a localized center. Notably, oscillators with positive and negative intrinsic frequencies, which correspond to opposite chiralities in the present model, are predominantly separated into different rotating groups. This indicates that the double-vortex configuration reflects a spatial segregation of mobile oscillators with opposite chiralities [43]. Correspondingly, the global order parameter $R_G(t)$, shown in Fig. 1(e), displays pronounced and regular oscillations over time, reflecting persistent collective dynamics while the system has not yet reached a fully synchronized state. As shown in Fig. 1(f), the adjacency matrix reveals a clear differentiation in neighbor connectivity. Interactions between different groups are still present, while neighbor connectivity mainly forms groups associated with spatially separated rotating regions.

At a stronger coupling strength $K = 2.5$, which lies above the critical threshold $K_c \approx 2$ associated with the instability of the incoherent state in the classical Kuramoto model for a Lorentzian frequency distribution with unit half-width, the system does not evolve toward a polar ordered state but instead remains in a vortex state. As shown in Fig. 1(g), a double-vortex configuration can still be identified in the spatial snapshot, although the two vortices exhibit a pronounced asymmetry in their spatial appearance. One vortex core is compact and clearly defined, whereas the other, located near the system boundary, is more diffuse yet still displays recognizable rotational organization. Correspondingly, the global order parameter, shown in Fig. 1(h), continues to exhibit regular oscillations throughout the observation window, with a larger amplitude than that observed at $K = 1$, indicating persistent collective dynamics rather than convergence to a phase-locked state. As seen in Fig. 1(i), the neighbor connectivity at $K = 2.5$ remains grouped, with interactions occurring primarily within each rotating group and relatively fewer connections between groups. Thus, even beyond the classical Kuramoto instability threshold, the system supports a persistent vortex state characterized by ongoing phase evolution rather than static synchronization.

At strong coupling $K = 6.5$, the system reaches a polar ordered state. As shown in Fig. 1(j), the spatial snapshot indicates that most oscillators move in nearly the same direction.

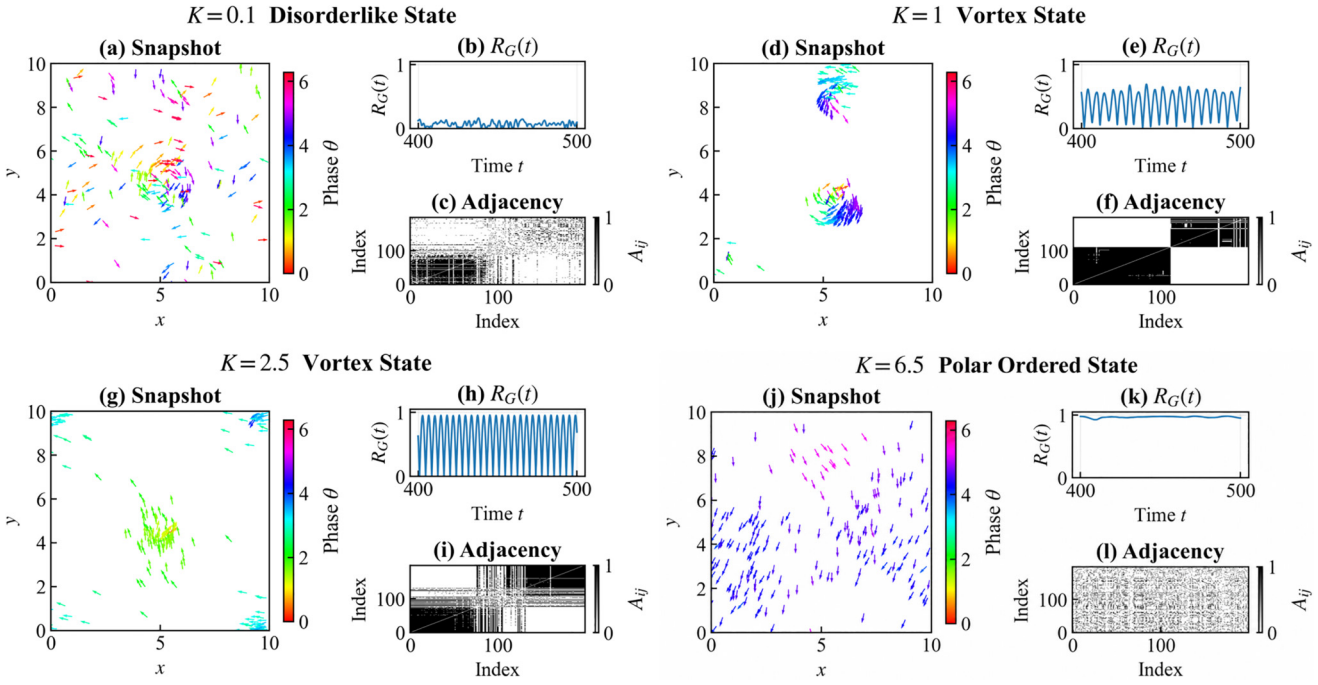


FIG. 1. Spatiotemporal patterns of the Vicsek-Kuramoto model for $d_0 = 2$ at different coupling strengths K. For each value of the coupling strength K, we present a snapshot of the emergent pattern, the time evolution of the global order parameter, and the corresponding adjacency matrix A_{ij}. Arrows indicate the instantaneous directions of motion of mobile phase oscillators, and their colors represent the phase θ, as shown by the color bar on the right. Numerical simulations are performed using the Euler method with a time step $dt = 0.01$ and a total integration time of $t = 50\,000$. Natural frequencies follow a Lorentzian distribution with half-width $\Delta = 1$. The remaining parameters are fixed as $L = 10$, $v = 0.5$, and $N = 200$. Panels (a)–(c) show the disorderlike state at $K = 0.1$, (d)–(f) the vortex state at $K = 1$, (g)–(i) the vortex state at $K = 2.5$, and (j)–(l) the polar ordered state at $K = 6.5$. Panels (a), (d), (g), and (j) show snapshots of the emergent patterns; (b), (e), (h), and (k) show the time evolution of the global order parameter $R_G(t)$; and (c), (f), (i), and (l) show the corresponding adjacency matrices A_{ij}.

The oscillators are distributed across the domain without forming rotational structures or localized clusters, and the overall motion appears highly coherent. Correspondingly, the global order parameter shown in Fig. 1(k) remains close to unity throughout the observation window, with only small fluctuations, indicating stable macroscopic coherence. From the adjacency matrix shown in Fig. 1(l), oscillators in the polar ordered state have similar numbers of neighbors. Compared with the vortex states, the interactions no longer exhibit clear grouping, but are instead more evenly spread among oscillators.

B. Persistence of vortex states

To understand under what conditions the previously observed vortex states emerge and persist, we systematically explore the dependence of the collective patterns on d_0 and K. Figure 2 summarizes the final patterns obtained for different combinations of the interaction range d_0 and the coupling strength K. As d_0 increases, the system exhibits pronounced changes in its spatial organization, indicating a gradual shift from locally organized motion to more globally coordinated behavior.

For small interaction ranges $d_0 = 1$ and $d_0 = 2$, oscillators interact only within a limited neighborhood. In the panels to the left of the red dashed boundary, the spatial snapshots show localized rotational structures rather than globally aligned motion. For $d_0 = 1$, these rotational patterns appear fragmented and confined to small regions, and vortex configurations are observed throughout the explored range of coupling strengths. When the interaction range increases to $d_0 = 2$, the rotational structures become more clearly visible and occupy slightly larger areas, although they remain spatially separated. As the coupling strength K increases within this regime, these localized vortex patterns continue to appear before the system transitions to polar ordered states in the panels to the right of the dashed boundary.

For intermediate interaction ranges $d_0 = 3$ and $d_0 = 4$, the spatial patterns display a different organization compared with the small-d_0 cases. Although rotational structures can still be identified in the panels to the left of the red dashed boundary, they no longer dominate the overall pattern and occupy a smaller portion of the domain. At the same time, larger regions with similar orientation begin to emerge, reducing the directional contrast across space. As K increases further, these coherent regions gradually replace the rotating structures, and the system enters polar ordered states in the panels to the right of the dashed boundary.

For sufficiently large interaction ranges $d_0 \geqslant 5$, interactions extend over a broad neighborhood. In this case, Fig. 2 shows that once the coupling strength exceeds $K \approx 2$, the previously observed vortex structures rapidly disappear. The oscillator phases tend toward synchronization, and the system transitions to a polar ordered state. In this polar ordered

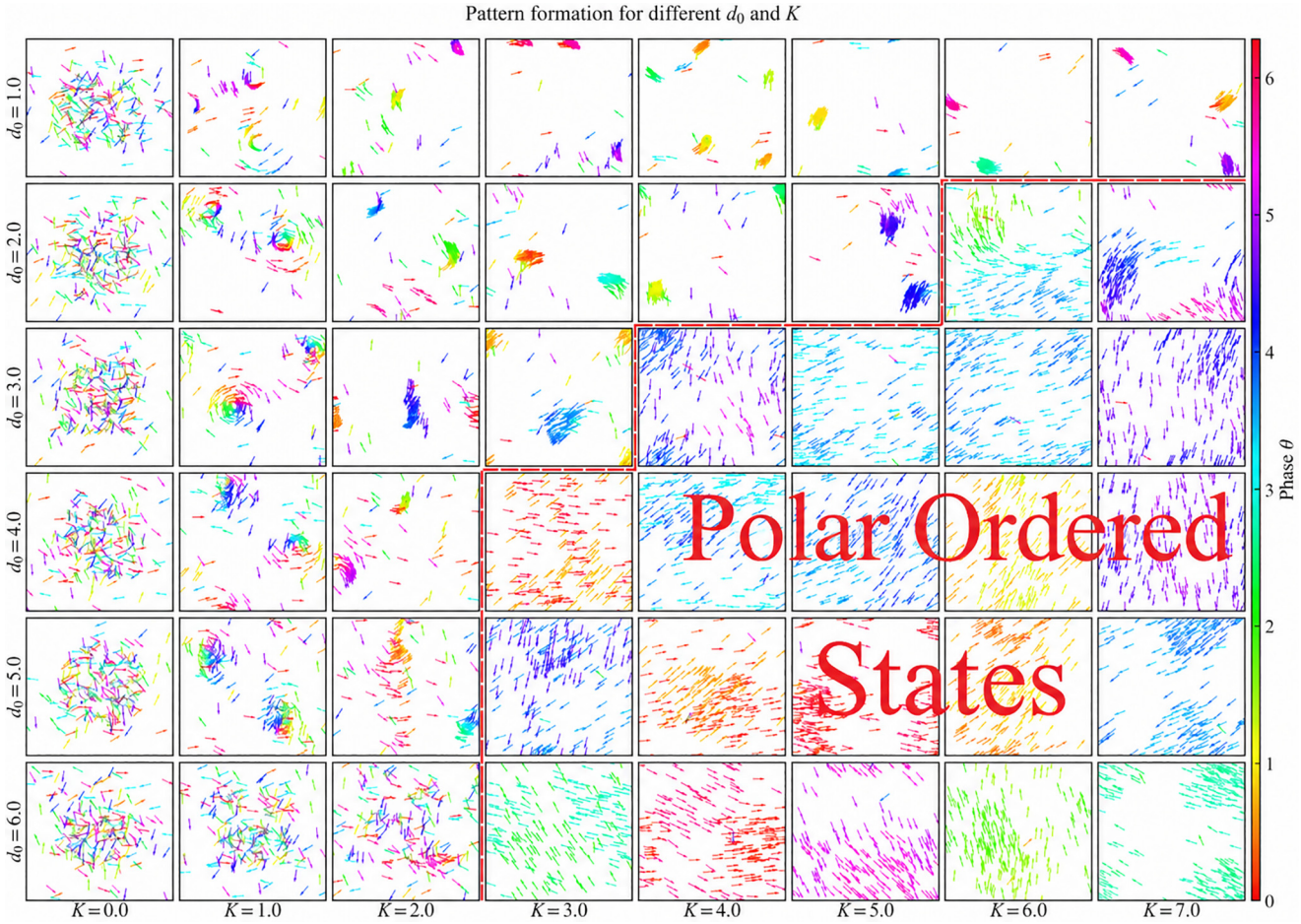


FIG. 2. Instantaneous pattern snapshots for different interaction ranges d_0 and coupling strengths K. Each row corresponds to a fixed interaction range d_0, increasing from top to bottom, while each column corresponds to a fixed coupling strength K, increasing from left to right. The regions to the right of the red dashed boxes correspond to polar ordered states. It can be seen that the transition from vortex states to polar ordered states occurs at different values of K for different d_0.

regime, the velocity directions become highly coherent across the entire domain, and rotational structures are strongly suppressed in the spatial patterns.

Overall, Fig. 2 demonstrates that the interaction range d_0 plays a key role in shaping the observed patterns. Small d_0 favors localized rotational structures, whereas large d_0 promotes globally aligned motion. Notably, the transition from vortex-dominated patterns to polar ordered states occurs at different coupling strengths for different interaction ranges, indicating that the location of the transition boundary depends on d_0. This observation shows that varying d_0 effectively shifts the parameter region in which polar ordered states are realized.

IV. VORTEX STATES AS STABLE ATTRACTORS

To clarify how the vortex state responds to slow variations of the coupling strength K and to examine the possible coexistence of multiple dynamical states, we perform adiabatic scans of the coupling strength for different interaction ranges d_0. Specifically, we adiabatically increase and decrease the coupling strength K and monitor the evolution of the global order parameter R_G, which is obtained by averaging over the last 2000 time steps once the system has reached a stationary state. Distinct critical coupling strengths are observed for the transition from the vortex state to the polar ordered state during the adiabatic increase of K and for the reverse transition during the adiabatic decrease. This gives rise to hysteresis regions whose widths depend on d_0, as shown in Fig. 3. The blue (orange) curve represents the evolution of R_G under the adiabatic increase (decrease) of K.

When $d_0 = 1$, the order parameter R_G increases smoothly with K and saturates at $R_G \approx 0.6$. Apart from minor numerical fluctuations, the forward and backward scans nearly overlap over the entire parameter range, indicating neither pronounced hysteresis nor bistability. In this regime, the system transitions from the disordered state to the vortex state, while no polar ordered state is observed.

For $d_0 = 2$, hysteresis emerges for $K \gtrsim 7.5$, indicating the coexistence of the vortex and polar ordered states over a finite but narrow parameter interval. Under adiabatic decrease of the coupling strength, the system follows the polar ordered branch with $R_G \approx 1$ and remains aligned down to lower values of K. Under adiabatic increase, it instead remains on the vortex branch with $R_G \approx 0.6$ throughout the explored parameter range.

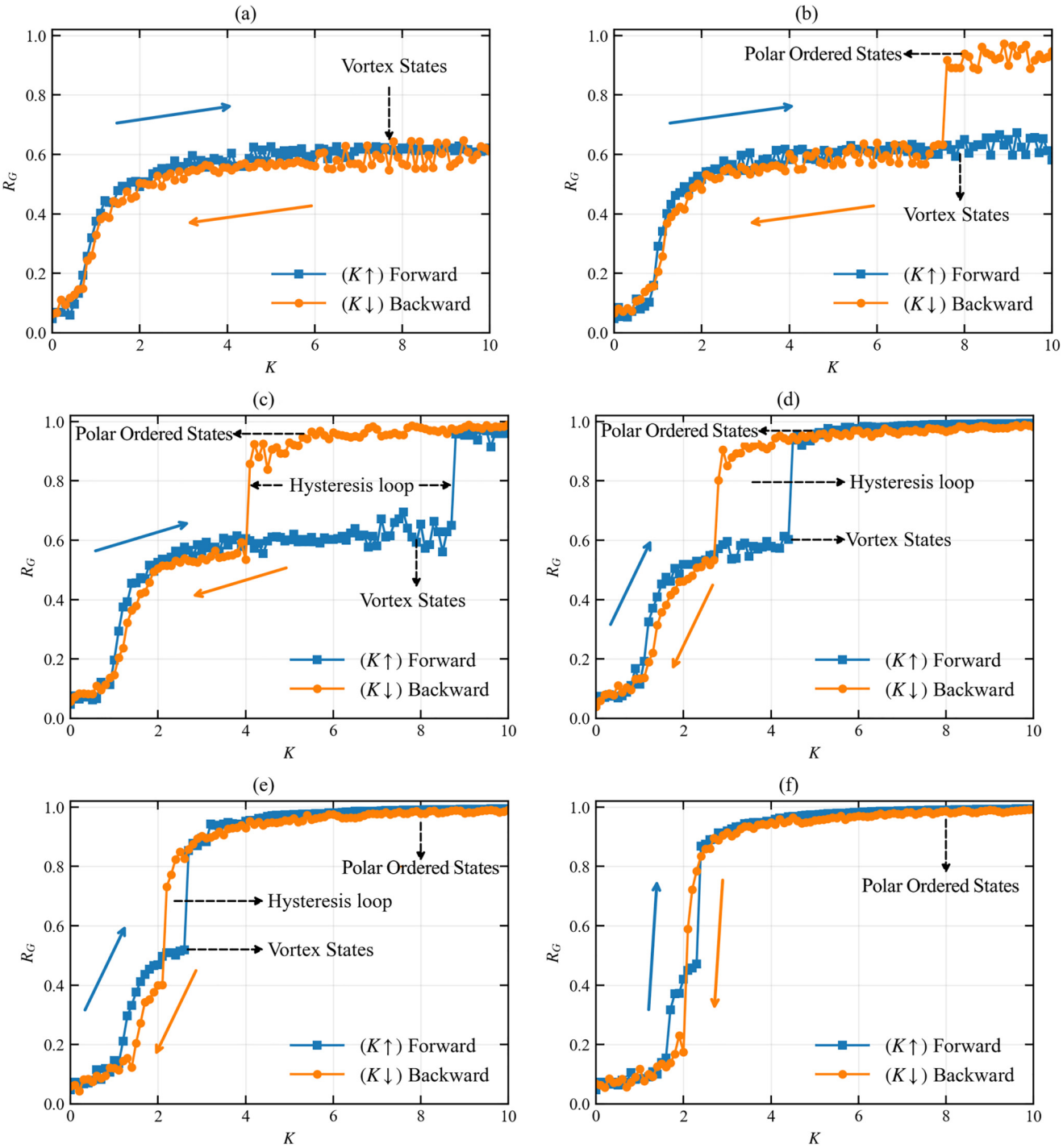


FIG. 3. Adiabatic scanning results of the global order parameter R_G as a function of the coupling strength K for different interaction ranges d_0. Panels (a)–(f) correspond to $d_0 = 1, 2, 3, 4, 5$, and 6, respectively. The blue curves show the evolution of R_G during the adiabatic increase of K, while the orange curves correspond to the adiabatic decrease of K. For small values of d_0, the system predominantly exhibits vortex states, and the forward and backward branches nearly overlap. As d_0 increases, discontinuous transitions between vortex states and polar ordered states emerge, accompanied by pronounced hysteresis loops whose widths depend on d_0. Arrows and dashed lines indicate different dynamical states and the associated hysteresis regions.

For $d_0 = 3$, the attractor landscape becomes significantly richer. For $2 \lesssim K \lesssim 4$, R_G forms a plateau at approximately 0.6, and the forward and backward scans nearly coincide, corresponding to a robust vortex attractor characterized by a long-lived vortex-antivortex pair without global alignment. For $K \gtrsim 4$, the two branches separate and the polar ordered state becomes dynamically accessible. The resulting bistable interval $4 \lesssim K \lesssim 8.5$ produces a hysteresis window substantially wider than that observed for $d_0 = 2$.

At $d_0 = 4$, the coexistence of the vortex and polar ordered states persists, but over a markedly reduced interval:

Upon increasing K, the vortex state is replaced by the polar ordered state at $K \approx 4.3$, whereas upon decreasing K, the polar ordered state remains stable down to $K \approx 2.8$. The closer transition thresholds demonstrate that the hysteresis window contracts substantially as the interaction range increases.

At $d_0 = 5$, a small hysteresis loop remains near $K \approx 2$, and vortex states are observed over a narrow coupling interval. At larger coupling strengths, the adiabatic scans follow the polar ordered branch. At $d_0 = 6$, the branch separation essentially disappears, the forward and backward scans nearly coincide over the entire parameter range, and the system undergoes a sharp yet reversible transition directly from a weakly ordered regime to the polar ordered state, indicating that multistability is lost when the interaction range becomes sufficiently large.

In summary, increasing the interaction range d_0 drives a qualitative change in the system dynamics. At small d_0, the evolution is reversible and no hysteresis is observed. At intermediate interaction ranges, vortex and polar ordered states coexist, leading to pronounced path dependence and hysteresis. As d_0 is further increased, the hysteresis window progressively shrinks and eventually disappears, and the system undergoes a direct and reversible transition to the polar ordered state. The hysteresis observed in the adiabatic scans provides numerical evidence for the coexistence of persistent vortex and polar ordered states over a finite coupling interval. The state reached depends on the direction of adiabatic continuation. These results support the interpretation of vortex states as dynamical attractors under the simulation conditions examined.

V. MECHANISM OF VORTEX STATES' PERSISTENCE

In Sec. III, we observe an intriguing phenomenon related to the interaction range d_0. When $d_0 \geqslant 5$, once the coupling strength K exceeds the critical value 2Δ corresponding to the classical Kuramoto model, the system does not exhibit a delayed vortex state but instead directly transitions into the polar ordered state. In contrast, for locally interacting oscillators with $d_0 \leqslant 5$, the vortex state can persist even when K exceeds 2Δ, and the smaller the interaction range d_0, the larger the coupling strength required for the transition from the vortex state to the polar ordered state. These observations indicate that the persistence of vortex states cannot be explained solely by the classical mean-field synchronization threshold. Instead, it is necessary to examine how the finite interaction range modifies the competition between spatially homogeneous synchronization and spatially modulated collective motion. In this section, we investigate the dynamical mechanism underlying this phenomenon.

A. Linear stability analysis of the disordered state

To elucidate why local interactions allow vortex states to persist beyond the classical Kuramoto critical coupling strength, we perform a linear stability analysis of the disordered state. We introduce the probability density function $f(\mathbf{x}, \theta, \omega, t)$ [58], which satisfies

$$\int_{\mathbb{R}^2} \int_{-\infty}^{\infty} \int_0^{2\pi} f(\mathbf{x}, \theta, \omega, t)\, d\theta\, d\omega\, d^2x = N. \tag{8}$$

In the disordered state, the oscillators are uniformly distributed in space. In this case, it satisfies

$$f_0 = \frac{N}{L^2} \times \frac{g(\omega)}{2\pi} = \rho_0 \frac{g(\omega)}{2\pi}. \tag{9}$$

To analyze the stability of the disordered state, we expand the distribution $f(x, \theta, \omega, t)$ in Fourier modes with respect to θ [49]:

$$f(\mathbf{x}, \theta, \omega, t) = \frac{\rho_0 g(\omega)}{2\pi} \sum_m F_m(\mathbf{x}, \omega, t) e^{im\theta}. \tag{10}$$

In the disordered state, one has $F_0 = 1$ and $F_m = 0$ for all $m \neq 0$.

Since the disordered state is spatially homogeneous and the interaction kernel depends only on the distance between oscillators, the linearized dynamics are invariant under spatial translations. As a result, a perturbation with a given wave vector does not generate components with different wave vectors at the linear level. We therefore consider solutions of the form

$$F_m(\mathbf{x}, \omega, t) = e^{\lambda t} e^{i\mathbf{q}\cdot\mathbf{x}} f_m(\omega), \tag{11}$$

where λ denotes the growth rate and $\mathbf{q}$ is the wave vector.

In the limit of a sufficiently large number of oscillators, the number of neighbors is given by $N_i = \rho_0 \pi d_0^2$. The corresponding perturbation of the local order parameter in Eq. (7) can be obtained as

$$\tilde{Z}(\mathbf{x}, t) = \frac{1}{\rho_0 \pi d_0^2} \int W(r)\, e^{i\theta'}\, \delta f(\theta', \omega', \mathbf{x}', t)\, d\theta'\, d\omega'\, d^2x', \tag{12}$$

where $r = d_{ij}$ denotes the spatial distance between oscillators i and j. The function $W(r)$ acts as a local interaction kernel that restricts the spatial coupling to a finite neighborhood, and is defined as

$$W(r) = \begin{cases} 1, & r \leqslant d_0, \\ 0, & r > d_0. \end{cases} \tag{13}$$

Since $\int_0^{2\pi} e^{i(m+1)\theta}\, d\theta = 2\pi\, \delta_{m,-1}$, only the $m = -1$ angular harmonic contributes to the perturbation of the local order parameter. Moreover, by absorbing the factor πd_0^2 into the interaction kernel, we introduce the normalized kernel $W'(r)$. As a result, the perturbation of the local order parameter can be written as

$$\tilde{Z}(\mathbf{x}, t) = e^{\lambda t} \left[\int_{\mathbb{R}^2} W'(r)\, e^{i\mathbf{q}\cdot\mathbf{x}'}\, d^2x' \right] \left[\int_{-\infty}^{\infty} g(\omega)\, f_{-1}(\omega)\, d\omega \right]. \tag{14}$$

Let $H(\mathbf{x}, \mathbf{q}, d_0)$ denote the spatial convolution term on the right-hand side of Eq. (14). Introducing $\mathbf{r} = \mathbf{x} - \mathbf{x}'$, we have $\mathbf{x}' = \mathbf{x} - \mathbf{r}$ and $e^{i\mathbf{q}\cdot\mathbf{x}'} = e^{i\mathbf{q}\cdot\mathbf{x}} e^{-i\mathbf{q}\cdot\mathbf{r}}$. For the normalized disk-shaped interaction kernel, $W'(r) = 1/(\pi d_0^2)$ for $r \leqslant d_0$ and $W'(r) = 0$ otherwise. Because the kernel is isotropic, we choose the polar axis along $\mathbf{q}$, so that $\mathbf{q} \cdot \mathbf{r} = qr \cos\phi$, with

$q = |\mathbf{q}|$. The spatial convolution then becomes

$$H(\mathbf{x}, \mathbf{q}, d_0) = \int_{\mathbb{R}^2} W'(|\mathbf{x} - \mathbf{x}'|) e^{i\mathbf{q}\cdot\mathbf{x}'} \, d^2\mathbf{x}' = \frac{e^{i\mathbf{q}\cdot\mathbf{x}}}{\pi d_0^2} \int_0^{d_0} r \, dr \int_0^{2\pi} e^{-iqr\cos\phi} \, d\phi. \quad (15)$$

The angular integral in Eq. (15) can be evaluated using the standard integral representation of J_0, the Bessel function of the first kind of order 0 [59]. This gives

$$\int_0^{2\pi} e^{-iqr\cos\phi} \, d\phi = 2\pi J_0(qr). \quad (16)$$

Substitution of Eq. (16) into Eq. (15) leaves a radial integral involving J_0. According to the standard differentiation property of Bessel functions, this integral can be reduced to a boundary term involving J_1, the Bessel function of the first kind of order 1. The lower boundary contribution vanishes because J_1 is regular at the origin. Hence,

$$\frac{2}{d_0^2} \int_0^{d_0} r J_0(qr) \, dr = \frac{2}{d_0^2} \left[\frac{r J_1(qr)}{q} \right]_0^{d_0} = \frac{2J_1(qd_0)}{qd_0} \equiv G(q, d_0). \quad (17)$$

Combining Eqs. (15)–(17) and substituting the result into Eq. (14), the perturbed local order parameter becomes

$$\widetilde{Z}(\mathbf{x}, t) = e^{\lambda t} e^{i\mathbf{q}\cdot\mathbf{x}} G(q, d_0) \int_{-\infty}^{\infty} g(\omega) f_{-1}(\omega) \, d\omega. \quad (18)$$

Here, $G(q, d_0)$ is the Fourier-space representation of the normalized interaction kernel. The apparent singularity at $q = 0$ is removable, and continuity gives $G(0) = 1$. Physically, $G(q, d_0)$ is the normalized Fourier transform of the circular interaction region. For $qd_0 \ll 1$, $G(q, d_0) \simeq 1 - (qd_0)^2/8$, so long-wavelength perturbations are transmitted almost unchanged. In contrast, when $qd_0 \gtrsim 1$, spatial variations within the interaction region partially cancel under local averaging, thereby attenuating finite-wave-number modes. The interaction kernel therefore acts as an effective spatial low-pass filter, with a characteristic cutoff wave number of order d_0^{-1}.

We adopt a continuum kinetic description in which position, orientation, and natural frequency are retained as distribution variables, following kinetic formulations of rotating active particles [60,61]. We adapt this description to the present noiseless model, with the coupling normalized by the number of neighbors. Within this continuum approximation, the distribution $f(\mathbf{x}, \theta, \omega, t)$ obeys

$$\frac{\partial f}{\partial t} + v \, \mathbf{n}(\theta) \cdot \nabla_{\mathbf{x}} f + \frac{\partial}{\partial \theta} [(\omega + K \, \mathrm{Im}(\tilde{Z} e^{-i\theta})) f] = 0, \quad (19)$$

where $\mathbf{n}(\theta) = (\cos\theta, \sin\theta)$. Following the kinetic approach to linear stability analysis for active particles with nonlocal angular coupling [62,63], we linearize Eq. (19) about the spatially homogeneous disordered state $f_0(\omega) = \rho_0 g(\omega)/(2\pi)$. Writing $f = f^{(0)} + \tilde{f}$, and retaining only first-order terms, the product $\tilde{Z}\tilde{f}$ is neglected. Owing to spatial isotropy, the wave vector can be chosen along the x direction without loss of generality. The linearized equation then reads

$$\frac{\partial \tilde{f}}{\partial t} + v\cos\theta \frac{\partial \tilde{f}}{\partial x} + \omega \frac{\partial \tilde{f}}{\partial \theta} + K \frac{\partial}{\partial \theta} [\mathrm{Im}(\tilde{Z} e^{-i\theta}) f^{(0)}] = 0. \quad (20)$$

Substituting Eqs. (10) and (11) into Eq. (20) yields the linearized angular-mode hierarchy. To obtain a closed analytical approximation, we retain only the lowest angular harmonics $m = 0, \pm 1$ and neglect the higher modes $|m| \geqslant 2$. The resulting coupled equations are

$$\begin{aligned} m = 0: &\quad \lambda f_0 + \frac{iqv}{2}(f_1 + f_{-1}) = 0, \\ m = 1: &\quad (\lambda + i\omega) f_1 + \frac{iqv}{2} f_0 = \frac{K}{2} \tilde{Z}^*, \\ m = -1: &\quad (\lambda - i\omega) f_{-1} + \frac{iqv}{2} f_0 = \frac{K}{2} \tilde{Z}. \end{aligned} \quad (21)$$

The $m = 0$ equation gives $f_0 = -iqv(f_1 + f_{-1})/(2\lambda)$. Substituting this relation into the $m = \pm 1$ equations yields

$$\begin{bmatrix} \lambda + i\omega + \alpha & \alpha \\ \alpha & \lambda - i\omega + \alpha \end{bmatrix} \begin{bmatrix} f_1 \\ f_{-1} \end{bmatrix} = \frac{K}{2} \begin{bmatrix} Z_\delta^* \\ Z_\delta \end{bmatrix}, \quad (22)$$

where $\alpha = \frac{q^2 v^2}{4\lambda}$ and

$$Z_\delta = G(q, d_0) \int_{-\infty}^{+\infty} f_{-1}(\omega) \, g(\omega) \, d\omega, \quad (23)$$

$$Z_\delta^* = G(q, d_0) \int_{-\infty}^{+\infty} f_1(\omega) \, g(\omega) \, d\omega. \quad (24)$$

Equation (22) is a 2×2 linear system for $f_1(\omega)$ and $f_{-1}(\omega)$. The determinant of its coefficient matrix is

$$D = \lambda^2 + 2\lambda\alpha + \omega^2. \quad (25)$$

According to the standard inverse formula, the two diagonal entries are interchanged, the signs of the off-diagonal entries are reversed, and the resulting matrix is divided by D. Multiplying this inverse matrix by the right-hand side of Eq. (22), the first and second rows give $f_1(\omega)$ and $f_{-1}(\omega)$, respectively, as

$$f_1(\omega) = \frac{K}{2} \frac{(\lambda - i\omega + \alpha) Z_\delta^* - \alpha Z_\delta}{D}, \quad (26)$$

$$f_{-1}(\omega) = \frac{K}{2} \frac{-\alpha Z_\delta^* + (\lambda + i\omega + \alpha) Z_\delta}{D}. \quad (27)$$

B. Lorentzian frequency analysis

The natural frequencies are assumed to follow the Lorentzian distribution with half-width Δ given in Eq. (5). Since $g(-\omega) = g(\omega)$ and the denominator D defined above depends on ω only through ω^2, both $g(\omega)$ and D are even functions of ω. Therefore,

$$\int_{-\infty}^{+\infty} \frac{\omega g(\omega)}{D} \, \mathrm{d}\omega = 0, \; I_0(\lambda, q) = \int_{-\infty}^{+\infty} \frac{g(\omega)}{D} \, \mathrm{d}\omega. \quad (28)$$

We first substitute Eq. (27) into Eq. (23). Separating the ω-independent and ω-dependent contributions gives

$$\begin{aligned} Z_\delta &= G(q,d_0)\int_{-\infty}^{+\infty} f_{-1}(\omega)g(\omega)\,\mathrm{d}\omega \\ &= \frac{K}{2}G(q,d_0)\int_{-\infty}^{+\infty}\frac{g(\omega)}{D}\{(\lambda+\alpha)Z_\delta-\alpha Z_\delta^*+i\omega Z_\delta\}\,\mathrm{d}\omega \\ &= \frac{K}{2}G(q,d_0)I_0(\lambda,q)[(\lambda+\alpha)Z_\delta-\alpha Z_\delta^*]. \end{aligned} \tag{29}$$

Likewise, substituting Eq. (26) into Eq. (24) yields

$$\begin{aligned} Z_\delta^* &= G(q,d_0)\int_{-\infty}^{+\infty} f_{1}(\omega)g(\omega)\,\mathrm{d}\omega \\ &= \frac{K}{2}G(q,d_0)\int_{-\infty}^{+\infty}\frac{g(\omega)}{D}\{(\lambda+\alpha)Z_\delta^*-\alpha Z_\delta-i\omega Z_\delta^*\}\,\mathrm{d}\omega \\ &= \frac{K}{2}G(q,d_0)I_0(\lambda,q)[(\lambda+\alpha)Z_\delta^*-\alpha Z_\delta]. \end{aligned} \tag{30}$$

Introducing $u=(K/2)G(q,d_0)I_0(\lambda,q)$, Eqs. (29) and (30) can be collected into the matrix self-consistency equation

$$\begin{bmatrix} u(\lambda+\alpha) & -u\alpha \\ -u\alpha & u(\lambda+\alpha)\end{bmatrix}\begin{bmatrix} Z_\delta \\ Z_\delta^*\end{bmatrix}=\begin{bmatrix} Z_\delta \\ Z_\delta^*\end{bmatrix}. \tag{31}$$

A nontrivial solution exists only if $(1-u\lambda-2u\alpha)(1-u\lambda)=0$, which yields two branches. The branch $1-u(\lambda+2\alpha)=0$ corresponds to the antisymmetric eigenvector $v_-=(1,-1)^\top$, which induces only a phase rotation of the order parameter and does not lead to a growth of its modulus. In contrast, the branch $1-u\lambda=0$ is associated with the symmetric eigenvector $v_+=(1,1)^\top$, which modifies the modulus of the order parameter. This mode characterizes the primary instability of the disordered state. Therefore, we obtain

$$1=\frac{K}{2}G(q,d_0)J(\lambda,q), \tag{32}$$

where $J(\lambda,q)=\lambda I_0(\lambda,q)$. Defining $A^2=\lambda^2+\frac{v^2q^2}{2}$, the integral $I_0(\lambda,q)$ can be written as

$$I_0(\lambda,q)=\int_{-\infty}^{+\infty}\frac{\Delta}{\pi(\omega^2+\Delta^2)}\times\frac{1}{\omega^2+A^2}d\omega. \tag{33}$$

To evaluate Eq. (33), we introduce the meromorphic function

$$F(z)=\frac{\Delta}{\pi(z^2+\Delta^2)(z^2+A^2)}. \tag{34}$$

We then close the integration contour with a semicircle in the upper half of the complex z plane. Since $F(z)=O(|z|^{-4})$ as $|z|\to\infty$, the contribution from the semicircular arc vanishes. The poles enclosed by the contour are $z=i\Delta$ and $z=iA$. For $A\neq\Delta$, the corresponding residues are

$$\mathrm{Res}\,[F(z),i\Delta]=\lim_{z\to i\Delta}(z-i\Delta)F(z)=\frac{1}{2\pi i(A^2-\Delta^2)} \tag{35}$$

and

$$\mathrm{Res}\,[F(z),iA]=\lim_{z\to iA}(z-iA)F(z)=-\frac{\Delta}{2\pi iA(A^2-\Delta^2)}. \tag{36}$$

Applying the residue theorem, we obtain

$$\begin{aligned} I_0(\lambda,q) &= 2\pi i[\mathrm{Res}\,(F,i\Delta)+\mathrm{Res}\,(F,iA)] \\ &= \frac{1}{A^2-\Delta^2}\left(1-\frac{\Delta}{A}\right)=\frac{1}{A(A+\Delta)}. \end{aligned} \tag{37}$$

For $A=\Delta$, the same expression follows from the continuous limit $A\to\Delta$. Consequently,

$$J(\lambda,q)=\frac{\lambda}{A(A+\Delta)}. \tag{38}$$

Combining Eqs. (32) and (38), we find that, for each fixed wave number q, the disordered state loses stability at the minimal coupling strength obtained by minimizing over the growth-rate parameter $\lambda>0$:

$$K_c(q)=\min_{\lambda>0}\frac{2\sqrt{\lambda^2+\frac{v^2q^2}{2}}\left(\sqrt{\lambda^2+\frac{v^2q^2}{2}}+\Delta\right)}{G(q,d_0)\,\lambda}. \tag{39}$$

For each fixed value of q, the critical value $K_c(q)$ is obtained by minimizing the expression above with respect to $\lambda>0$, which can be performed numerically. Due to the periodic boundary condition on a domain of length L, admissible perturbations satisfy $e^{iq(x+L)}=e^{iqx}$, which restricts the allowed wave numbers to

$$q_n=\frac{2\pi n}{L},\quad n\in\mathbb{Z}. \tag{40}$$

Therefore, in a finite system, one only needs to evaluate $K_c(q_n)$ on the discrete set $\{q_n\}$.

For the zero mode $n=0$, that is, $q=0$, the expansion of $J_1(x)$ near the origin implies

$$G(q,d_0)=\frac{2J_1(qd_0)}{qd_0}\to 1\quad\text{as } q\to 0. \tag{41}$$

Substituting this result and $q=0$ into Eq. (39), we obtain

$$K_c(0)=2\Delta. \tag{42}$$

This result agrees with the critical coupling for the instability of the disordered state in the classical Kuramoto model, demonstrating the consistency of the present dispersion relation with the standard Kuramoto theory. A direct analysis of Eq. (39) shows that $K_c(q)$ attains its minimum at $q=0$ and increases monotonically with increasing q. This result implies that the disordered state first loses stability through the uniform mode ($q=0$), and notably, this instability is independent of the interaction radius d_0. In contrast, for $q\neq 0$, the critical value $K_c(q_n)$ depends explicitly on the interaction range d_0 through the kernel $G(q,d_0)$, so that spatial modes with finite wave numbers are strongly influenced by the interaction range.

C. Mode competition with d_0

To quantify how close each spatial mode is to its linear instability threshold at a given coupling strength K, we introduce the relative coupling strength

$$S(q_n)=\frac{K}{K_c(q_n)}. \tag{43}$$

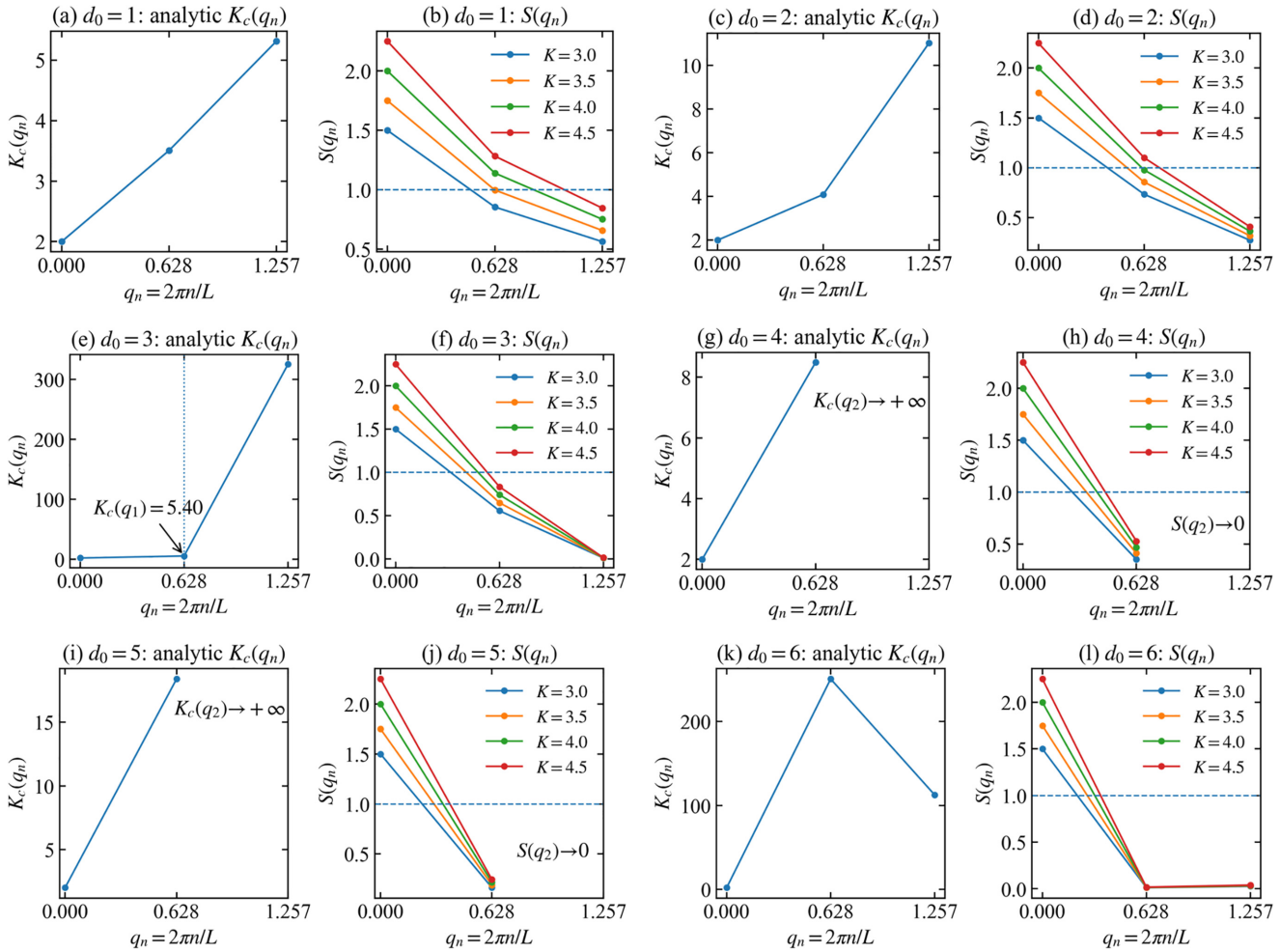


FIG. 4. Critical coupling strengths $K_c(q_n)$ and the corresponding relative coupling strengths $S(q_n)$ for different interaction ranges d_0. For each interaction range d_0, the left column shows the analytically obtained $K_c(q_n)$ as a function of the wave number $q_n = 2\pi n/L$, while the right column shows $S(q_n)$ for different values of the coupling strength K. The dashed line indicates $S(q_n) = 1$, which corresponds to the linear stability threshold. As d_0 increases, the critical coupling strengths associated with finite-wave-number modes increase significantly, and in some cases $K_c(q_n)$ diverges, resulting in $S(q_n) \to 0$ for finite values of K. Panels (a), (c), (e), (g), (i), and (k) show the analytically obtained critical coupling strengths $K_c(q_n)$ for $d_0 = 1, 2, 3, 4, 5, 6$, respectively. Panels (b), (d), (f), (h), (j), and (l) show the corresponding relative coupling strengths $S(q_n)$ for the same respective interaction ranges, with $K = 3.0, 3.5, 4.0, 4.5$.

When $S(q_n) > 1$, the mode with wave number q_n becomes linearly unstable. For $S(q_n) \leqslant 1$, the mode is linearly stable, since the real part of the growth rate remains negative, but it becomes small when $S(q_n)$ is close to one. By jointly examining the q dependence of $K_c(q_n)$ and the corresponding values of $S(q_n)$, we can systematically characterize how different spatial modes approach instability as the interaction radius d_0 is varied. Accordingly, $K_c(q_n)$ and $S(q_n)$ are computed numerically for different interaction radii d_0, as shown in Fig. 4.

For $d_0 = 1$, the lowest finite-wave-number threshold corresponds to q_1 and lies close to $K_c(q_0)$, whereas q_2 has a higher critical coupling, as shown in Fig. 4(a). At $K = 3$, $S(q_0) > 1$ while $S(q_1) < 1$. For $K = 3.5$, 4, and 4.5, $S(q_1)$ slightly exceeds unity, whereas $S(q_2)$ remains below unity throughout the same range, as shown in Fig. 4(b). Thus, although q_1 is not the first mode to become unstable, it can participate in the subsequent nonlinear dynamics together with the homogeneous mode.

For $d_0 = 2$, the homogeneous mode still loses stability at $K_c(q_0) = 2$, whereas the q_1 threshold increases to $K_c(q_1) \simeq 4$ and the q_2 threshold is still higher, as shown in Fig. 4(c). Within the interval $K \simeq 3$–4.5, q_1 remains linearly stable up to $K = 4$ and only slightly exceeds its threshold at $K = 4.5$, while q_2 remains stable, as shown in Fig. 4(d). Compared with $d_0 = 1$, the finite-wave-number instability therefore occurs at a larger coupling strength, although q_1 can still influence the nonlinear evolution near its threshold.

For $d_0 = 3$, the q_1 threshold is further shifted to $K_c(q_1) = 5.4$, while q_2 has a substantially higher critical coupling, as shown in Figs. 4(e) and 4(f). Over the interval $K \simeq 3$–5, $S(q_1)$ remains below unity over most of the range, while q_2 lies even farther from instability. Nevertheless, vortex states and hysteresis are observed over the same parameter range. During the downward scan, the polar ordered state persists to $K \simeq 3.8$ before returning to the vortex state, as shown in Fig. 3(c). This behavior does not contradict the linear analysis, which

describes the stability of the incoherent state but does not exclude nonlinear spatial structures when finite-wave-number perturbations remain linearly damped.

For $d_0 = 4$, $K_c(q_1) \simeq 8$, whereas $K_c(q_2) \to +\infty$ and hence $S(q_2) \to 0$, as shown in Figs. 4(g) and 4(h). The q_1 mode remains below its threshold over the relevant coupling range, while the q_2 mode is effectively inactive. Vortex states nevertheless persist over a finite coupling-strength interval, but both their persistence range and the hysteresis window are substantially narrower than those for $d_0 = 3$, as shown in Fig. 3(d).

For $d_0 \geqslant 5$, vortex states are no longer observed above the homogeneous threshold $K_c(q_0) = 2\Delta$, and the system directly approaches the polar ordered state. At $d_0 = 5$, the finite-wave-number thresholds are already much larger than the homogeneous threshold, as shown in Figs. 4(i) and 4(j). At $d_0 = 6$, $K_c(q_1) \simeq 260$ and $K_c(q_2) \simeq 120$, yielding $S(q_n) < 1$ for all finite wave numbers considered, as shown in Figs. 4(k) and 4(l).

Comparing the results for different interaction radii shows that d_0 modifies the instability conditions of spatially nonuniform perturbations around the incoherent state while leaving the homogeneous threshold unchanged. Within the parameter range examined, increasing d_0 raises the instability threshold of the lowest finite-wave-number mode, eventually placing it beyond the coupling range considered. The separation between these thresholds characterizes the linear instability spectrum of the incoherent state. Its connection to the numerically observed vortex persistence interval is heuristic and does not constitute a quantitative prediction of that interval.

VI. DEPENDENCE OF COLLECTIVE STATES ON PARTICLE NUMBER AND SYSTEM SIZE

We performed additional adiabatic scans of the Vicsek-Kuramoto model for $N = 400, 600, 800, 1000$, and 1200 at fixed $L = 10$, using the same parameter grid as the original $N = 200$ simulations (see Figs. S1–S5 of the Supplemental Material (SM) [64]).

All five scans show similar overall state distributions, including disordered configurations, localized vortices and associated clusters, and polar ordered states. The polar ordered regions coincide exactly on the sampled grid, while localized vortices and clusters at smaller interaction radii remain observable even for $N = 1200$. For $d_0 \geqslant 4$, all five scans exhibit direct entry into polar order at the sampled couplings above the homogeneous-mode critical coupling $K_c(0) = 2\Delta$, with no persistent intermediate vortex state. These results support the qualitative robustness of this ordering pattern beyond the original $N = 200$ system, across the tested particle numbers and scanning conditions.

To examine domain enlargement at fixed density, we additionally scanned $(N, L) = (450, 15)$ and $(800, 20)$, maintaining the original density $\rho = N/L^2 = 2$ (see Figs. S6 and S7 of the SM [64]). Both enlarged systems remain disordered at $K = 0$, and the localized vortices and clusters at $d_0 = 1, 2$ persist as in the earlier scans. At $d_0 = 3$, the $L = 20$ snapshots retain separated clusters at $K = 5, 6, 7$, whereas the $L = 15$ snapshots show spatially extended polar configurations. At $d_0 = 4, 5$, the enlarged scans differ from the fixed-L results, which already exhibit polar order at $K = 3$. For $d_0 = 4$, the first sampled couplings exhibiting polar order are $K = 4$ for $L = 15$ and $K = 6$ for $L = 20$. For $d_0 = 5$, the $L = 15$ system is polar ordered at $K = 3$, while the $L = 20$ system remains clustered; both exhibit polar order at $K = 5, 6, 7$.

At $d_0 = 6$, both enlarged systems reproduce the original ordering pattern: Polar order at every sampled coupling $K = 3$–7, with no persistent intermediate vortex state. Here, $K = 3$ is the first sampled value above $K_c(0) = 2\Delta = 2$. In the derived dispersion relation, d_0 enters the linear instability conditions through the normalized local interaction-kernel factor $G(q, d_0)$. The enlarged-domain results at $d_0 = 6$ are consistent with these conditions and show that polar ordering does not require the interaction neighborhood to cover the entire simulation domain.

These comparisons show that the sampled intermediate-state regions at $d_0 = 3$–5 change with domain enlargement, while the pattern of direct entry into polar order at $d_0 = 6$ is retained on the sampled grid. Together with the fixed-L particle-number scans, these results support the qualitative robustness of the ordering behavior at $d_0 = 6$ and its interpretation in terms of the local interaction kernel, indicating that this phenomenon is not a finite-size artifact specific to the original small system with $N = 200$, $L = 10$.

VII. DISCUSSION

We have investigated how the interaction radius affects persistent vortex states and their transition to polar order in the Vicsek-Kuramoto model. Within the parameter range examined, increasing the interaction radius narrows the coupling interval supporting vortices, while adiabatic scans reveal coexistence and hysteresis between vortex and polar ordered states. These observations highlight the spatial extent of local interactions as a relevant parameter for collective rotation.

Within the present continuum linear approximation, the homogeneous incoherent state first becomes unstable at $K_c(0) = 2\Delta$, independently of the interaction radius, whereas the instability thresholds of perturbations at finite wave numbers depend on the spatial interaction kernel. These results characterize perturbation growth around the incoherent state, but do not determine the selection or stability of the collective states that subsequently develop. The connection between the linear instability spectrum and vortex persistence therefore remains heuristic. A quantitative account of vortex stability boundaries, hysteresis, and selection among coexisting states requires nonlinear analysis.

To address this gap, future work could explore a description involving multiple scales for the coupled evolution of particle motion and collective phase order. This idea is motivated by the feedback between particle transport, the evolving interaction neighborhood, and local synchronization, which may involve different characteristic timescales. Distinguishing these processes could provide a framework for examining how initial perturbation growth develops into persistent spatial organization and how the interaction radius influences this evolution.

If a suitable separation of scales can be established, the Ginzburg-Landau framework could offer a unified description of nonlinear saturation and spatial modulation. This approach may help clarify how collective rotation is sustained and how vortex states coexist with polar order. It could also provide a basis for exploring whether persistent vortex patterns are associated with stable collective oscillations, thereby connecting the temporal evolution of collective order with its spatial organization. The applicability of this framework to the present model remains to be established in future work.

ACKNOWLEDGMENTS

We are grateful to members in the group for stimulating discussions. This work was partially supported by National Natural Science Foundation of China (Grants No. 12375031 and No. 11875135).

DATA AVAILABILITY

There are no publicly available research data or software supporting this manuscript. Requests for further information or data should be sent to the authors.

[1] K. Wiesenfeld, P. Colet, and S. H. Strogatz, Synchronization transitions in a disordered Josephson series array, Phys. Rev. Lett. **76**, 404 (1996).

[2] Y. Kuramoto, Chemical turbulence, in *Chemical Oscillations, Waves, and Turbulence*, edited by H. Haken (Springer, Berlin, 1984), pp. 111–140.

[3] M. Zhang, G. S. Wiederhecker, S. Manipatruni, A. Barnard, P. McEuen, and M. Lipson, Synchronization of micromechanical oscillators using light, Phys. Rev. Lett. **109**, 233906 (2012).

[4] R. Yang, Y. Wang, X. Wang, Z. Lei, Z. Zheng, and Y. Qian, The extended master stability function approach to alternating synchronization modes on networked oscillator systems, New J. Phys. **28**, 013901 (2026).

[5] M. Rohden, A. Sorge, M. Timme, and D. Witthaut, Self-organized synchronization in decentralized power grids, Phys. Rev. Lett. **109**, 064101 (2012).

[6] S. H. Strogatz, D. M. Abrams, A. McRobie, B. Eckhardt, and E. Ott, Crowd synchrony on the Millennium Bridge, Nature (London) **438**, 43 (2005).

[7] J. R. Terry, K. S. Thornburg, D. J. DeShazer, G. D. VanWiggeren, S. Zhu, P. Ashwin, and R. Roy, Synchronization of chaos in an array of three lasers, Phys. Rev. E **59**, 4036 (1999).

[8] A. Cavagna, A. Cimarelli, I. Giardina, G. Parisi, R. Santagati, F. Stefanini, and M. Viale, Scale-free correlations in starling flocks, Proc. Natl. Acad. Sci. USA **107**, 11865 (2010).

[9] M. Ballerini, N. Cabibbo, R. Candelier, A. Cavagna, E. Cisbani, I. Giardina, A. Orlandi, G. Parisi, A. Procaccini, M. Viale, and V. Zdravkovic, Empirical investigation of starling flocks: A benchmark study in collective animal behaviour, Anim. Behav. **76**, 201 (2008).

[10] I. D. Cousin, J. Krause, R. James, G. D. Ruxton, and N. R. Franks, Collective memory and spatial sorting in animal groups, J. Theor. Biol. **218**, 1 (2002).

[11] J. E. Herbert-Read, A. Perna, R. P. Mann, T. M. Schaerf, D. J. T. Sumpter, and A. J. W. Ward, Inferring the rules of interaction of shoaling fish, Proc. Natl. Acad. Sci. USA **108**, 18726 (2011).

[12] I. H. Riedel, K. Kruse, and J. Howard, A self-organized vortex array of hydrodynamically entrained sperm cells, Science **309**, 300 (2005).

[13] A. C. Quillen, A. Peshkov, B. Chakrabarti, N. Skerrett, S. McGaffigan, and R. Zapiach, Fluid circulation driven by collectively organized metachronal waves in swimming *T. aceti* nematodes, Phys. Rev. E **106**, 064401 (2022).

[14] A. Barciś, M. Barciś, and C. Bettstetter, Robots that sync and swarm: A proof of concept in ROS 2, in *2019 International Symposium on Multi-Robot and Multi-Agent Systems (MRS)* (IEEE, Piscataway, NJ, 2019), pp. 98–104.

[15] J. Toner and Y. Tu, Long-range order in a two-dimensional dynamical XY model: How birds fly together, Phys. Rev. Lett. **75**, 4326 (1995).

[16] J. Toner and Y. Tu, Flocks, herds, and schools: A quantitative theory of flocking, Phys. Rev. E **58**, 4828 (1998).

[17] J. Toner, Y. Tu, and S. Ramaswamy, Hydrodynamics and phases of flocks, Ann. Phys. **318**, 170 (2005).

[18] K. Tunstrøm, Y. Katz, C. C. Ioannou, C. Huepe, M. J. Lutz, I. D. Couzin, and E. Ben-Jacob, Collective states, multistability and transitional behavior in schooling fish, PLoS Comput. Biol. **9**, e1002915 (2013).

[19] J. K. Parrish, S. V. Viscido, and D. Grünbaum, Self-organized fish schools: An examination of emergent properties, Biol. Bull. **202**, 296 (2002).

[20] C. Huang, F. Ling, and E. Kanso, Collective phase transitions in confined fish schools, Proc. Natl. Acad. Sci. USA **121**, e2406293121 (2024).

[21] D. H. Kelley and N. T. Ouellette, Emergent dynamics of laboratory insect swarms, Sci. Rep. **3**, 1073 (2013).

[22] J. Jhawar, V. Guttal, and S. Thutupalli, Stochastic dynamics of order and disorder in milling whirligig beetles, Phys. Rev. Res. **7**, 043308 (2025).

[23] X. Wang and J. Lu, Collective behaviors through social interactions in bird flocks, IEEE Circuits Syst. Mag. **19**, 6 (2019).

[24] I. D. Couzin and N. R. Franks, Self-organized lane formation and optimized traffic flow in army ants, Proc. R. Soc. Lond. B **270**, 139 (2003).

[25] T. C. Schneirla, A unique case of circular milling in ants, considered in relation to trail following and the general problem of orientation, Am. Mus. Novit. **1253**, 1 (1944).

[26] H. Wioland, F. G. Woodhouse, J. Dunkel, J. O. Kessler, and R. E. Goldstein, Confinement stabilizes a bacterial suspension into a spiral vortex, Phys. Rev. Lett. **110**, 268102 (2013).

[27] E. Lushi, H. Wioland, and R. E. Goldstein, Fluid flows created by swimming bacteria drive self-organization in confined suspensions, Proc. Natl. Acad. Sci. USA **111**, 9733 (2014).

[28] J. Dunkel, S. Heidenreich, K. Drescher, H. H. Wensink, M. Bär, and R. E. Goldstein, Fluid dynamics of bacterial turbulence, Phys. Rev. Lett. **110**, 228102 (2013).

[29] H. P. Zhang, A. Be'er, E.-L. Florin, and H. L. Swinney, Collective motion and density fluctuations in bacterial colonies, Proc. Natl. Acad. Sci. USA **107**, 13626 (2010).

[30] Y. Kuramoto, Self-entrainment of a population of coupled nonlinear oscillators, in *International Symposium on Mathematical Problems in Theoretical Physics: January 23–29, 1975, Kyoto University, Kyoto, Japan* (Springer, Berlin, 1975), pp. 420–422.

[31] S. H. Strogatz, From Kuramoto to Crawford: Exploring the onset of synchronization in populations of coupled oscillators, Physica D **143**, 1 (2000).

[32] J. A. Acebrón, L. L. Bonilla, C. J. P. Vicente, F. Ritort, and R. Spigler, The Kuramoto model: A simple paradigm for synchronization phenomena, Rev. Mod. Phys. **77**, 137 (2005).

[33] T. Vicsek, A. Czirók, E. Ben-Jacob, I. Cohen, and O. Shochet, Novel type of phase transition in a system of self-driven particles, Phys. Rev. Lett. **75**, 1226 (1995).

[34] T. Vicsek and A. Zafeiris, Collective motion, Phys. Rep. **517**, 71 (2012).

[35] F. Ginelli, The physics of the Vicsek model, Eur. Phys. J.: Spec. Top. **225**, 2099 (2016).

[36] A. Chepizhko and V. Kulinskii, On the relation between Vicsek and Kuramoto models of spontaneous synchronization, Physica A **389**, 5347 (2010).

[37] B. Ventejou, H. Chaté, R. Montagne, and X. Shi, Susceptibility of orientationally ordered active matter to chirality disorder, Phys. Rev. Lett. **127**, 238001 (2021).

[38] Y. Wang, B. Ventéjou, H. Chaté, and X. Shi, Condensation and synchronization in aligning chiral active matter, Phys. Rev. Lett. **133**, 258302 (2024).

[39] N. Kruk, J. A. Carrillo, and H. Koeppl, Traveling bands, clouds, and vortices of chiral active matter, Phys. Rev. E **102**, 022604 (2020).

[40] K. P. O'Keeffe, H. Hong, and S. H. Strogatz, Oscillators that sync and swarm, Nat. Commun. **8**, 1504 (2017).

[41] K. P. O'Keeffe, J. H. M. Evers, and T. Kolokolnikov, Ring states in swarmalator systems, Phys. Rev. E **98**, 022203 (2018).

[42] S. Ceron, K. O'Keeffe, and K. Petersen, Diverse behaviors in non-uniform chiral and non-chiral swarmalators, Nat. Commun. **14**, 940 (2023).

[43] Y. Lu, Y. Xu, W. Cai, Z. Tian, J. Xu, S. Wang, T. Zhu, Y. Liu, M. Wang, Y. Zhou, C. Yan, C. Li, and Z. Zheng, Self-organized circling, clustering and swarming in populations of chiral swarmalators, Chaos Solit. Fractals **191**, 115794 (2025).

[44] X. Xu, Y. Lu, S. Wang, J. Xu, and Z. Zheng, Collective dynamics of swarmalators driven by a mobile pacemaker, Chaos **34**, 113103 (2024).

[45] M. Ballerini, N. Cabibbo, R. Candelier, A. Cavagna, E. Cisbani, I. Giardina, V. Lecomte, A. Orlandi, G. Parisi, A. Procaccini, M. Viale, and V. Zdravkovic, Interaction ruling animal collective behavior depends on topological rather than metric distance: Evidence from a field study, Proc. Natl. Acad. Sci. USA **105**, 1232 (2008).

[46] A. Ziepke, I. Maryshev, I. S. Aranson, and E. Frey, Multi-scale organization in communicating active matter, Nat. Commun. **13**, 6727 (2022).

[47] M. C. Marchetti, J. F. Joanny, S. Ramaswamy, T. B. Liverpool, J. Prost, M. Rao, and R. A. Simha, Hydrodynamics of soft active matter, Rev. Mod. Phys. **85**, 1143 (2013).

[48] D. Sumpter, The principles of collective animal behaviour, Philos. Trans. R. Soc. B **361**, 5 (2006).

[49] B. Liebchen and D. Levis, Collective behavior of chiral active matter: Pattern formation and enhanced flocking, Phys. Rev. Lett. **119**, 058002 (2017).

[50] B. Liebchen and D. Levis, Chiral active matter, Europhys. Lett. **139**, 67001 (2022).

[51] K. O'Keeffe, G. K. Sar, M. S. Anwar, J. U. F. Lizárraga, M. A. M. de Aguiar, and D. Ghosh, A solvable two-dimensional swarmalator model, Proc. R. Soc. A **480**, 20240448 (2024).

[52] G. K. Sar, K. O'Keeffe, and D. Ghosh, Effects of coupling range on the dynamics of swarmalators, Phys. Rev. E **111**, 024206 (2025).

[53] V. L. Heuthe, P. Iyer, G. Gompper, and C. Bechinger, Tunable colloidal swarmalators with hydrodynamic coupling, Nat. Commun. **16**, 10984 (2025).

[54] G. Vásárhelyi, C. Virágh, G. Somorjai, T. Nepusz, A. E. Eiben, and T. Vicsek, Optimized flocking of autonomous drones in confined environments, Sci. Rob. **3**, eaat3536 (2018).

[55] L. Zhou, S. Leng, Q. Wang, and Q. Liu, Integrated sensing and communication in UAV swarms for cooperative multiple targets tracking, IEEE Trans. Mob. Comput. **22**, 6526 (2022).

[56] E. Yanmaz, S. Yahyanejad, B. Rinner, H. Hellwagner, and C. Bettstetter, Drone networks: Communications, coordination, and sensing, Ad Hoc Networks **68**, 1 (2018).

[57] K. Meng, Q. Wu, J. Xu, W. Chen, Z. Feng, R. Schober, and A. L. Swindlehurst, UAV-enabled integrated sensing and communication: Opportunities and challenges, IEEE Wirel. Commun. **31**, 97 (2024).

[58] E. Bertin, M. Droz, and G. Grégoire, Hydrodynamic equations for self-propelled particles: Microscopic derivation and stability analysis, J. Phys. A: Math. Theor. **42**, 445001 (2009).

[59] *NIST Handbook of Mathematical Functions*, edited by F. W. J. Olver, D. W. Lozier, R. F. Boisvert, and C. W. Clark (Cambridge University Press, New York, 2010), p. 223.

[60] P. Degond, G. Dimarco, and T. B. N. Mac, Hydrodynamics of the Kuramoto–Vicsek model of rotating self-propelled particles, Math. Models Methods Appl. Sci. **24**, 277 (2014).

[61] M. F. Ivarsen, Polar chiral active matter as a motile, disordered Josephson array: Information supercurrents and Goldstone spin waves, Phys. Rev. E **114**, 035417 (2026).

[62] D. Escaff and R. Delpiano, Flocking transition within the framework of Kuramoto paradigm for synchronization: Clustering and the role of the range of interaction, Chaos **30**, 083137 (2020).

[63] D. Escaff, Instabilities and the emergence of self-organization in active matter: General considerations and an example, Chaos **35**, 073114 (2025).

[64] See Supplemental Material at http://link.aps.org/supplemental/10.1103/mzgk-nx4w for additional adiabatic parameter scans at fixed system size and at fixed number density, as detailed in Figs. S1–S7 and Table S1.